Chapter 2
Theoretical Background

The fundamentals of Spectro-Spatial Interferometry (Mariotti and Ridgway 1988), also called Double Fourier Modulation (DFM) or Multi-Fourier Transform Spectroscopy (Ohta et al. 2007, 2006), are presented here and provide the background for the understanding of the following chapters.

The goal of Double Fourier Modulation is to measure the spectral and spatial characteristics of an object simultaneously and it can be understood as the combination of two well known techniques: Fourier transform spectroscopy (FTS) and Stellar Interferometry. The literature regarding both FTS and Stellar Interferometry is extensive, and the concepts presented here are the ones related to the work of this Thesis.

In Sect. 2.1 the theoretical background of Fourier Transform Spectroscopy is presented. The starting point is the Michelson Interferometer, as the design of many interferometers used today are based on the Michelson original design from 1891. Special emphasis is after given to the generation and sampling of the interferograms, as a correct measurement of a source spectrum is strongly related to the selection of the instrument parameters. Finally the procedure for the recovery of the spectrum is described.

In Sect. 2.2 the fundamentals of Stellar Interferometry are shown. Starting with the Young's double slit experiment the interferometric observables are explained, this is, the complex visibility function. The data synthesis relevant to the work of this thesis is then presented. Finally, in Sect. 2.3 the concept of Multi-Fourier Transform Interferometry is developed.

R. Juanola-Parramon, *A Far-Infrared Spectro-Spatial Space Interferometer*,
Springer Theses, DOI 10.1007/978-3-319-29400-1_2

2.1 Fourier Transform Spectroscopy

Fourier Transform Spectroscopy (FTS) is a widely used technique (Griffiths and de Haseth 2007) based on the Michelson interferometer for the determination of the spectral distribution of a source. The light of a source is divided and recombined after delaying one of the optical paths as a function of time to generate an interferogram recorded with a detector. This interferogram is consequently Fourier transformed to obtain the source spectral distribution. In this section the principles of operation of the Fourier transform spectrograph are presented, with emphasis on the sampling of the interferogram and the spectrum reconstruction algorithms.

2.1.1 The Michelson Interferometer

The design of many interferometers used for infrared spectrometry today is based on that of the two-beam interferometer originally designed by Michelson (1891a, b, 1903) in 1891. The Michelson interferometer is a device that generates an interference pattern by splitting a beam of light into two paths and recombining them. The introduced spatial delay of one of the optical paths causes the appearance of fringes by forcing constructive or destructive interference. By recording the power at different spatial positions an interferogram is acquired.

Figure 2.1 shows the simplest form of a Michelson interferometer. It consists of two perpendicular plane mirrors, one fixed and one movable to introduce the required

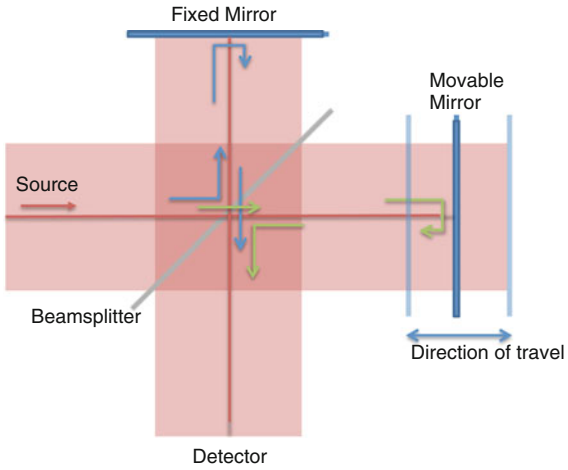

Fig. 2.1 The simplest Michelson interferometer, consisting of two mutually perpendicular plane mirrors, one of which can move along an axis that is perpendicular to its plane. A collimated light source (*red*) reaches the beamsplitter, which splits the light in two paths: reflected (*blue arrow*) and transmitted (*green arrow*). The fixed mirror reflects the light back to the beamsplitter, and the movable mirror reflects the transmitted light to the beamsplitter, where they interfere

delay, and a beamsplitter. The beamsplitter partially reflects and partially transmits a collimated beam of radiation from an external source. The beams then return to the beamsplitter where they interfere and are again partially reflected and partially transmitted.

The optical path difference (OPD) between the beams that travel to the fixed and movable mirror and back to the beamsplitter is called retardation, δ. When the path length on both arms of the interferometer are equal, the position of the moving mirrors is referred to as the position of zero retardation or zero path difference (ZPD). The two beams are perfectly in phase on recombination at the beamsplitter, where the beams interfere constructively and the intensity of the beam passing to the detector is the sum of the intensities of the beams passing to the fixed and movable mirrors. Therefore, all the light from the source reaches the detector at this point and none returns to the source. To understand why no radiation returns to the source at ZPD one has to consider the phases on the beam splitter.

2.1.1.1 Phases on the Beam Splitter

A beam that is reflected by a mirror at normal incidence undergoes a phase change of π. However, the phase difference between the reflected and the transmitted beams from a beam splitter is $\pi/2$: the beam that is reflected undergoes a phase change of $\pi/2$ while the phase of the transmitted beam remains unchanged (Lawson 2000). In this section this statement is proved.

First consider an ideal, thin and symmetric beam splitter. The relative amplitude and phase shift of the reflected wavefront are r and δ_r, and the relative amplitude and phase shift of the transmitted wavefront are t and δ_t, respectively.

The source emits a beam with amplitude E_0 which is split into a reflected complex amplitude $re^{i\delta_r}$ and a transmitted complex amplitude $te^{i\delta_t}$. Each beam is reflected by a perfectly reflecting mirror and returned to the beam splitter, where the beams each split again. The output or emerging amplitudes towards the detector (E_d) and towards the source (E_s) are

$$\begin{aligned} E_d &= E_0 re^{i\delta_r} te^{i\delta_t} + E_0 te^{i\delta_t} re^{i\delta_r} \\ &= 2rtE_0 e^{i(\delta_r+\delta_t)} \end{aligned} \tag{2.1}$$

$$\begin{aligned} E_s &= E_0 re^{i\delta_r} re^{i\delta_r} + E_0 te^{i\delta_t} te^{i\delta_t} \\ &= E_0 \left[r^2 e^{i2\delta_r} + t^2 e^{i2\delta_t} \right] \end{aligned} \tag{2.2}$$

The corresponding intensities of the incident beam (I_0) and the emerging beam (I_d and I_s) are

$$I_0 = E_0 E_0^* = |E_0|^2 \tag{2.3}$$

$$I_d = E_d E_d^* = |E_0|^2 4RT \tag{2.4}$$

$$I_s = E_s E_s^* = |E_0|^2 \left[(R-T)^2 + 4RT\cos^2(\delta_r - \delta_t) \right] \tag{2.5}$$

where $R = |r^2|$ and $T = |t^2|$. Conservation of energy requires that $I_0 = I_d + I_s$. In this scenario, the phase shift is

$$\begin{aligned} \cos^2(\delta_r - \delta_t) &= 0 \\ |\delta_r - \delta_t| &= \pi/2 \end{aligned} \tag{2.6}$$

Thus the reflected and transmitted beam from a thin beam splitter will present a $\pi/2$ phase shift between them.

The overall phases of the system are as follow: the beam to the detector that travels to the fixed mirror undergoes a $\pi/2$ phase change on the beam splitter, a π phase change on the fixed mirror, and no phase change at the beam splitter, $3\pi/2$ in total. The transmitted beam to the detector undergoes no phase change when transmitted through the beam splitter, π phase change on the movable mirror and $\pi/2$ phase change when reflected by the beam splitter, again $3\pi/2$ in total. Therefore, the beams are in phase and interfere constructively. The beam travelling back to the source from the fixed mirror undergoes a $\pi/2$ at the beam splitter, a π phase change at the fixed mirror and a second $\pi/2$ phase change on the beam splitter, 2π phase change in total. From the movable mirror, the beam undergoes only the mirror phase change, π. Thus, the two beams are π radiants out of phase and interfere destructively. For this reason, at the ZPD the entire power of the incident beam is transmitted to the detector and no light returns to the source.

2.1.2 Generating the Interferogram

By displacing the movable mirror one alters the retardation between the beams. If the mirror is displaced a distance $\lambda/4$, the optical path difference between the beams on the beamsplitter is $\lambda/2$ and the beams interfere destructively as they are out of phase. In this situation, all the light returns to the source. Likewise, if the retardation is λ (corresponding to a mirror displacement of $\lambda/2$), the beams interfere constructively on the beam splitter, and all the light travels to the detector.

In the case of monochromatic light of wavelength λ_0 (or wavenumber $\nu_0 = 1/\lambda_0$), as shown in Fig. 2.2, the intensity of the beam at the detector measured as a function of retardation has a cosine shape, where the maximums correspond to retardation intervals multiple of λ_0. At other wavenumbers ν, the intensity of the beam at the detector is

$$I_d(\delta) = 2RTI_0(\nu)(1 + \cos 2\pi\nu\delta) \tag{2.7}$$

As seen in Eq. 2.4, for the particular case of the ZPD where $\delta = 0$, the intensity of the beam at the detector is $I_d(\delta) = 4RTI_0(\nu)$. Considering an ideal beam splitter ($R = T = 1/2$) this equation becomes

$$I_d(\delta) = \frac{1}{2} I_0(\nu)(1 + \cos 2\pi\nu\delta) \tag{2.8}$$

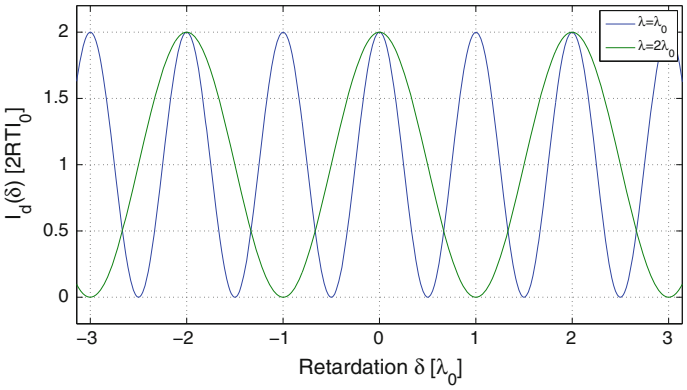

Fig. 2.2 Interference pattern for monochromatic light of wavelength λ_0 (*blue*) and $2\lambda_0$ (*green*) as a function of the retardation δ (in units of λ_0). The maxima corresponds to retardation intervals multiple of λ_0 and $2\lambda_0$, respectively

where a dc component equal to $\frac{I_0(\nu)}{2}$ and a modulated component $\frac{I_0(\nu)}{2}\cos 2\pi\nu\delta$ can be observed. In spectroscopy only the ac component is used in general, and is referred to as the interferogram.

For a broadband source $B(\nu)$, where radiation of more than one wavelength is emitted by the source, the measured interferogram is the result of the sum of the cosines contributions corresponding to each wavenumber, in other words, a measure of the interference of all the spectral components of $B(\nu)$ as the retardation is varied. In this situation the measured interferogram is

$$I_d(\delta) = \int_{-\infty}^{\infty} B(\nu)\cos(2\pi\nu\delta)d\nu \tag{2.9}$$

which is the cosine Fourier transform (or the real part of the Fourier transform). By performing the inverse cosine Fourier transform, one can recover the spectral information of the source, this is

$$B(\nu) = \int_{-\infty}^{\infty} I_d(\delta)\cos(2\pi\nu\delta)d\delta \tag{2.10}$$

$B(\nu)$ is an even function and it can be written as

$$B(\nu) = 2\int_{0}^{\infty} I_d(\delta)\cos(2\pi\nu\delta)d\delta \tag{2.11}$$

which means that in theory one could measure the complete spectrum from 0 to ∞ at infinitely high spectral resolution.

Figure 2.3 shows a representation of the generation of an interferogram for a broadband source with a flat spectrum.

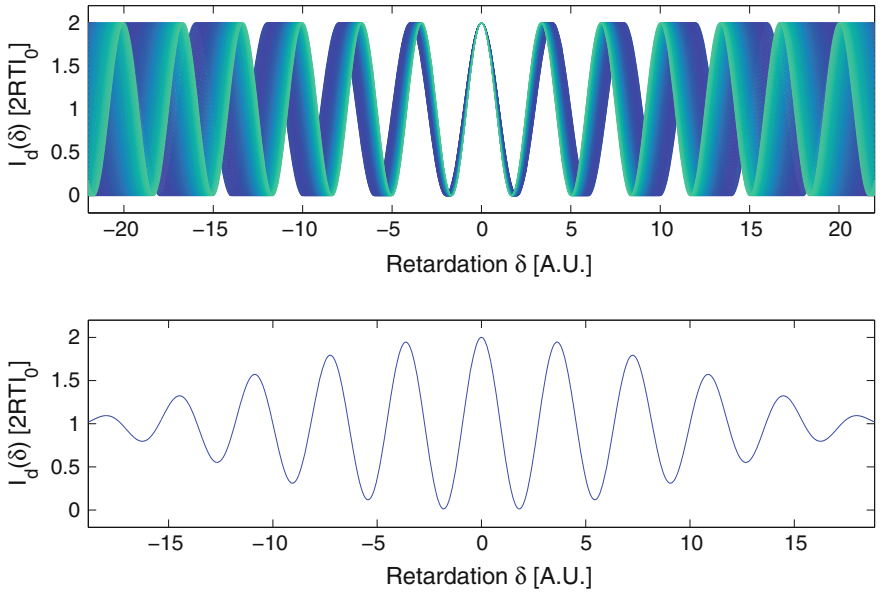

Fig. 2.3 Individual monochromatic responses (*top*) and the resulting interferogram (*bottom*) for a broadband (or polychromatic) source

In theory, by scanning an infinite distance one could recover the spectrum at infinitely high resolution. In practice one selects a maximum optical path difference to be scanned, limiting the spectral resolution of the measurement.

2.1.3 Sampling the Interferogram

Interferograms are sampled at equal intervals of retardation x, which mathematically is the multiplication of an analog interferogram by a repetitive impulse function, the Dirac comb, given by

$$\text{Ш}(x) = \sum_{n=-\infty}^{\infty} \delta(x - n\Delta x) \tag{2.12}$$

where Δx is the sampling interval. The Fourier transform of the Dirac delta comb is another Dirac delta comb of period $1/\Delta x$, that is

$$\text{Ш}(\nu) = \sum_{n=-\infty}^{\infty} \delta(\nu - \frac{n}{\Delta x}) \tag{2.13}$$

In the Fourier domain, the spectra are convolved with the Dirac delta comb (Eq. 2.13), which means the spectrum will be infinitely repeated. To avoid aliasing, if the spectrum covers a bandwidth from 0 to ν_{max}, the transformed Dirac delta comb must have a period of at least $2\nu_{max}$, this is

$$\Delta x \leq \frac{1}{2\nu_{max}} \tag{2.14}$$

Under this condition, which is known as the *Nyquist criterion*, the analog signal may be digitised without any loss of information.

2.1.3.1 Effect of Finite Path Difference

By sampling a finite path difference Δ another instrumental effect is introduced to the interferogram. Effectively, the complete interferogram (from $-\infty$ to ∞) is multiplied by a boxcar truncation function, $D(x)$, which is

$$D(x) = \begin{cases} 1 & \text{if } -\Delta \leq x \leq \Delta \\ 0 & \text{if } x > |\Delta| \end{cases}$$

In the spectral domain, it is equivalent to the convolution of the spectra $B(\nu)$ with the Fourier transform of $D(x)$, which is

$$\begin{aligned} f(\nu) &= 2\Delta \frac{\sin 2\pi\nu\Delta}{2\pi\nu\Delta} \\ &= 2\Delta \operatorname{sinc} 2\pi\nu\Delta \end{aligned} \tag{2.15}$$

and it is also called the *Instrument Line Shape* function (ILS). For any spectrometer, the ILS defines the shape of a spectral line given a monochromatic input.

2.1.3.2 Spectrometer Resolution

When the spectrum to be measured corresponds to a single spectral line of wavenumber ν_1, this is $B_1(\nu) = \delta(\nu - \nu_1)$ the recovered spectrum is

$$B(\nu) = B_1(\nu) * f(\nu) = 2\Delta \operatorname{sinc} 2\pi(\nu - \nu_1)\Delta \tag{2.16}$$

Figure 2.4 shows the instrumental line shape, $f(\nu)$ (top), and $B(\nu)$ (bottom) for $\nu_1 = 2/\Delta$. Looking at the ILS, it can be observed that the curve intersects the wavenumber axis at $\pm 1/2\Delta$, and for $B(\nu)$ the intersection happens at $\nu_1 \pm 1/2\Delta$. In this situation, two spectral lines separated by twice this amount $(1/\Delta)$ will be completely resolved.

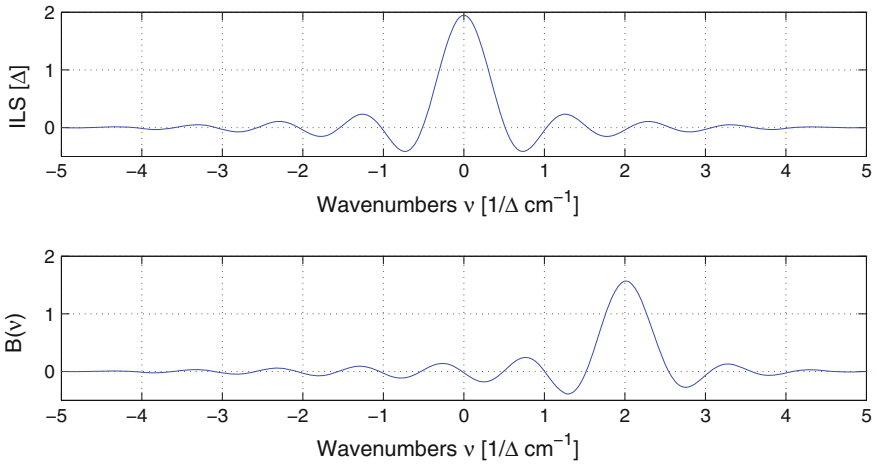

Fig. 2.4 Instrumental Line Shape $ILS(\nu)$ (*top*), which is the Fourier transform of a boxcar function of unit amplitude extending from $+\Delta$ to $-\Delta$. Fourier transform of an interferogram generated by a monochromatic line at $\nu_1 = 2/\Delta$ (*bottom*)

However, the practical resolution is better than this value. Considering the full width at half maximum (FWHM) criterion, two spectral lines will be resolved if the spacing between lines is greater than the FWHM of either line, this is

$$\Delta\nu = \frac{1.207}{2\Delta} \tag{2.17}$$

which is valid for a sinc-like ILS. The ILS can be modified through *apodization*, which can be useful to reduce the side lobes of the ILS by weighting the interferogram but can also affect the photometric accuracy.

2.1.4 Recovering the Spectrum

The relationship between an interferogram and the corresponding spectrum is the Fourier transform (or cosine transform, as the interferogram is real). However, the interferogram is discretely sampled and finite. For this reason, a *discrete Fourier transform* (DFT) needs to be performed.

The general definition of the DFT is

$$B(\boldsymbol{\nu}) = \sum_{n=0}^{N-1} I_d(\delta_n) e^{-2\pi \boldsymbol{\nu} \delta_n / N} \tag{2.18}$$

where $\boldsymbol{\nu}$ is the wavenumber vector and N the number of elements of the interferogram $I_d(\boldsymbol{\delta})$. Given the maximum wavenumber defined by the Nyquist criterion, ν_{max}, the spectral resolution is

$$\Delta\nu = \frac{\nu_{max}}{N} \tag{2.19}$$

and as the sampling interval is $\Delta\delta = \Delta/N$, combining both expressions the spectral resolution can be written as

$$\Delta\nu = \frac{1}{2\Delta} \tag{2.20}$$

which is only valid if the ILS is not being considered.

2.1.4.1 Apodization

The convolution theorem (Goodman 2005) states that the Fourier transform of the multiplication of two functions in one domain is equivalent to the convolution in the other, as given by

$$\mathscr{F}^{-1}\{F(\nu)\cdot G(\nu)\} = f(x) * g(x) = \int_{-\infty}^{\infty} f(t)g(x-t)dt \tag{2.21}$$

where t is a dummy variable and $f(x) * g(x)$ denotes the convolution of $f(x)$ and $g(x)$.

Apodization is the modification of the interferogram by multiplication with an apodization function (Griffiths and de Haseth 2007). If the interferogram is unweighted, the shape of a spectral line is the convolution of the spectrum with a sinc function, which is the Fourier transform of the boxcar truncation function.

A sinc function introduces ringing in the spectrum because of the side lobes. By selecting a different apodization function, the side lobes can be reduced but at the cost of a loss of spectral resolution.

The most common apodization functions are those proposed by Norton and Beer (1976) and the triangle function (Griffiths and de Haseth 2007). Norton and Beer tested over 1000 functions of the general form

$$A(\delta) = \sum_{i=0}^{n} C_i \left[1 - \left(\frac{\delta}{\Delta}\right)^2\right]^i \tag{2.22}$$

and concluded that there is a distinct empirical boundary relation between the FWHM and the relative magnitude of the strongest side lobe to the central lobe. Three preferred functions are Norton-Beer weak, medium and strong apodization function.

Figure 2.5 shows three examples of apodization functions and the corresponding ILS. It can be observed that the triangular and squared triangular apodization functions (green and red, respectively) present a reduced side lobe intensity. However,

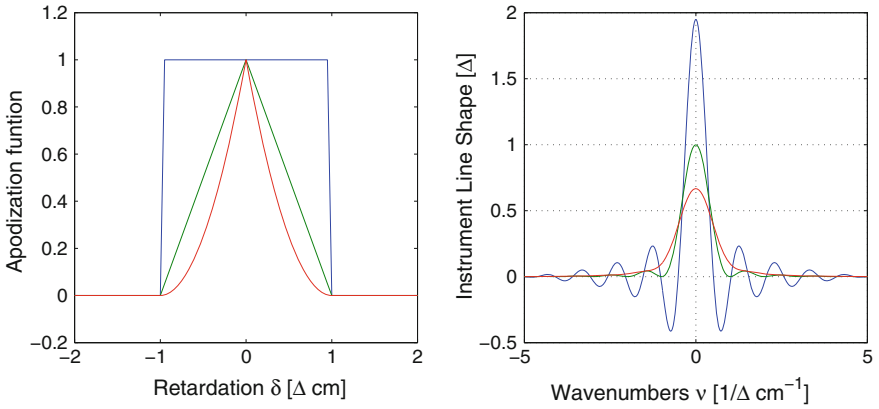

Fig. 2.5 Apodization functions (*left*) and corresponding Instrumental Line Shape (*right*) boxcar (*blue*), triangular (*green*) and squared triangular (*red*)

the spectral resolution is being decreased with respect to the boxcar apodization function.

2.1.4.2 Phase Effects

Until now, it has been assumed the interferogram to be perfectly symmetric or even. However, in practice an additional term often has to be added to the phase angle $2\pi\nu\delta$ to describe the measured interferogram.

Phase effects $\varphi(\nu)$ in the interferogram mainly appear because the zero path difference point is not accurately known or sampled, some dispersive phenomena exist in optical elements, and/or due to electronic filters used to reduce the bandwidth of the detector, which induce a wavenumber dependent phase lag. Under these circumstances, the interferogram can be written as

$$I(\delta) = 2\int_0^\infty B(\nu)\cos[2\pi\nu\delta + \varphi(\nu)]d\nu \tag{2.23}$$

$$= \int_{-\infty}^{\infty} B(\nu)e^{-i\varphi(\nu)}e^{-i2\pi\nu\delta}d\nu \tag{2.24}$$

where $\varphi(-\nu) = -\varphi(\nu)$ and the interferogram is no longer symmetric. The interferogram is now the Fourier transform of $S(\nu) = B(\nu)e^{-i\varphi(\nu)}$, which can also be written as

$$S(\nu) = B_r(\nu)\cos[\varphi(\nu)] - B_i(\nu)\sin[\varphi(\nu)] \tag{2.25}$$

where $B_r(\nu)$ and $B_i(\nu)$ represent the real and imaginary parts of $B(\nu)$.

2.1.4.3 Phase Correction

The process of phase correction consists of determining $\varphi(\nu)$ experimentally from the imaginary and the real parts of $S(\nu)$ and then multiplying through by $e^{i\varphi(\nu)}$ to recover $B(\nu)$, by using the fact that the phase error $\varphi(\nu)$ is a smooth function and does not vary rapidly with ν.

The Forman phase correction method (Forman et al. 1966) is one of the most used methods. Given an interferogram unequally sided by sampling from $-\Delta_1$ to Δ_2 (in order to increase the spectral resolution by increasing the total optical path difference), the Forman method first finds the ZPD and selects a region where the interferogram is double sided and the signal exceeds the noise, ZPD $\pm\, x$. This interferogram is then apodized with a triangular apodization function and by performing the Fourier transform the phase can be extracted. Once the phase is known, it is inverted and inverse Fourier transformed to create the convolution kernel. Next, the measured interferogram and the kernel are convolved. This process can be iterative, and eventually the convolution kernel resembles a delta function. This process is illustrated in Fig. 2.6.

2.2 Stellar Interferometry

An interferometer can be basically described as an instrument that measures the interference of an electromagnetic field. The advantage of interferometers over other instruments when measuring astronomical sources is the angular resolution achievable, providing means to address certain scientific questions not available to single aperture telescopes. In this Section the basic principles and characteristics of an ideal stellar interferometer are presented, as well as the interferometric observables and its synthesis (Born and Wolf 1999; Monnier 2003; Quirrenbach 2001).

2.2.1 Basic Principles

When using an interferometer one is measuring coherence functions (Haniff 2007). In this section the focus is on the spatial coherence function, which is the case associated with measuring the electric field from a source at two locations but at the same time. This is equivalent to the Young's two slit experiment.

2.2.1.1 The Young Experiment

The first experiment for demonstrating the interference of light is due to Young (1804). In his experiment, light from a monochromatic point source S falls on two pinholes, P_1 and P_2 which are close together on a screen and equidistant from S. The

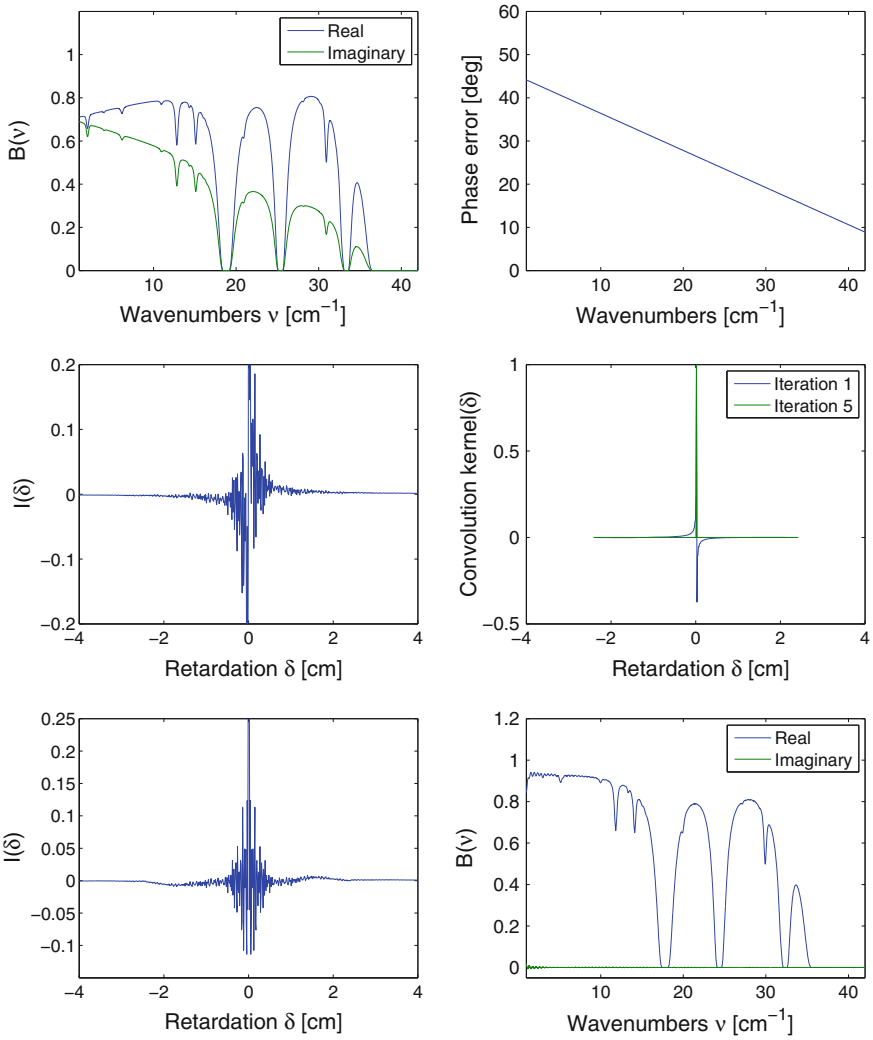

Fig. 2.6 Forman phase correction method. The real and imaginary part of the spectrum corresponding to the transmission of the atmosphere from 0 to 42 cm^{-1} has been distorted (*top-left*) with a linear phase error (*top-right*). The measured interferogram is not symmetric anymore (*centre-left*). After extracting the convolution kernel (*centre-right*) and applying the correction method 5 times, the interferogram symmetry is improved (*bottom-left*). Fourier transforming the corrected interferogram, the spectrum is recovered (*bottom-right*) and is real

separation between the two pinholes is the baseline, b. The pinholes act as secondary monochromatic point sources which are in phase, and the light is projected onto a screen beyond the pinholes screen and a pattern of fringes is observed.

The interference is due to the wave nature of light: the electric field at each slit is propagating to the screen with different relative path lengths, hence interfering constructively and destructively at different points along the screen. Figure 2.7 (left) shows a simple Young's two-slit interferometer response to a point source, where the interference fringe can be characterised by an amplitude and phase. For constructive interference, the fringe spacing $\Delta\Theta$ is proportional to the projected slit separation b in units of wavelength λ, this is

$$\Delta\Theta = \frac{\lambda}{b}\,\text{rad} \tag{2.26}$$

and the fringe spatial frequency is

$$u = \frac{b}{\lambda}\,\text{rad}^{-1} \tag{2.27}$$

If a second point source is located at an angle of $\lambda/(2b)$ from the first source, as in Fig. 2.7 (right) the two interference patterns are out of phase with one another by π rad and they cancel each other, as the fringe phase depends on the angle of the incoming wavefront: the measurement of fine phase is equivalent to a measurement of stellar position on the sky. On the screen, one would see a uniform illumination. The Young's experiment is a simple illustration of an interferometer having two telescopes in place of pinholes and subsequently combining the two beams for interference.

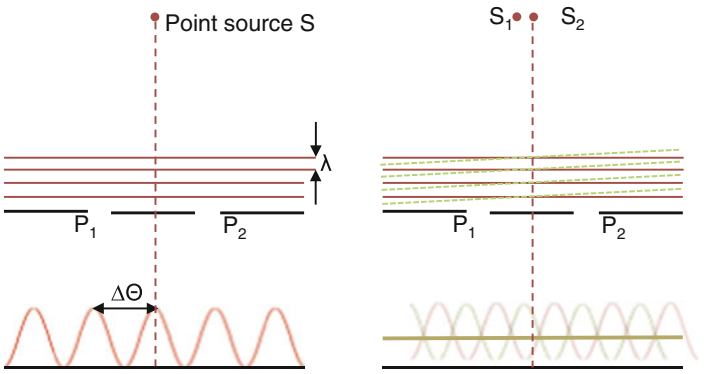

Fig. 2.7 The Young's two-slit interferometer response to a point source (*left*) is a pattern of fringes characterised by an amplitude and a phase. If a second point source is positioned at a distance $\lambda/(2b)$ from the initial source (*right*), the two interference patters are out of phase and cancel each other, allowing the measurement of the stellar position on the sky

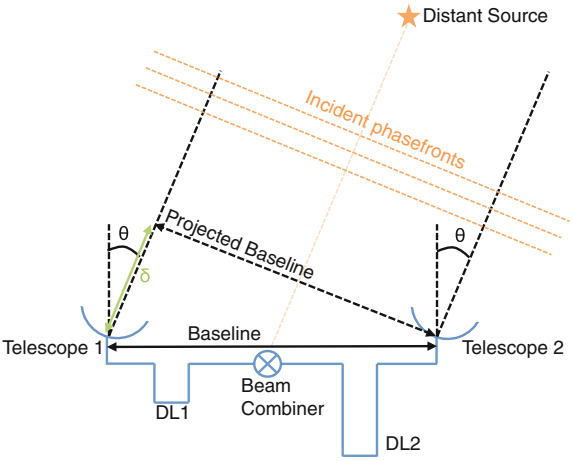

Fig. 2.8 Schematic of an interferometer. Two telescopes collect the light that then travels along the delay lines DL1 and DL2 and interferes at the beam combiner. The geometrical delay δ is compensated with the delay lines in order to find maximum fringe coherence to measure stellar positions. θ is the view angle

Figure 2.8 shows a basic representation of a 2 element interferometer. Two telescopes are separated by a physical distance, the baseline, and pointing towards a distant source at an angle θ from the meridian. By measuring the delay line required to find stellar fringes, the incoming angle of the wavefronts can be calculated and thus the stellar position on the sky.

2.2.1.2 Angular Resolution and Fringe Visibility

The angular (or spatial) resolution, is defined as the ability to discern two objects with an image-forming device. For an astronomical instrument the ability to distinguish the two components of a binary star is often used. Classical diffraction theory established the Rayleigh criterion for the definition of the diffraction limited resolution (Hecht 2001). According to the Rayleigh criterion, two sources will be resolved when one component is centred on the first null in the diffraction pattern of the other. In this case, given a circular aperture of diameter D, the angular resolution is

$$\Delta\theta_{Tel} = 1.220\frac{\lambda}{D}\,\text{rad} \tag{2.28}$$

If instead of the Rayleigh criterion the full width at half maximum (FWHM) criterium is considered, the angular resolution is $\Delta\theta_{Tel} = 1.02\lambda/D \approx \lambda/D$. For an interferometer, two equal brightness sources will be resolved when the fringe contrast goes to zero at the longest baseline b, this is

$$\Delta\theta_{Int} = \frac{\lambda}{2b}\,\text{rad} \tag{2.29}$$

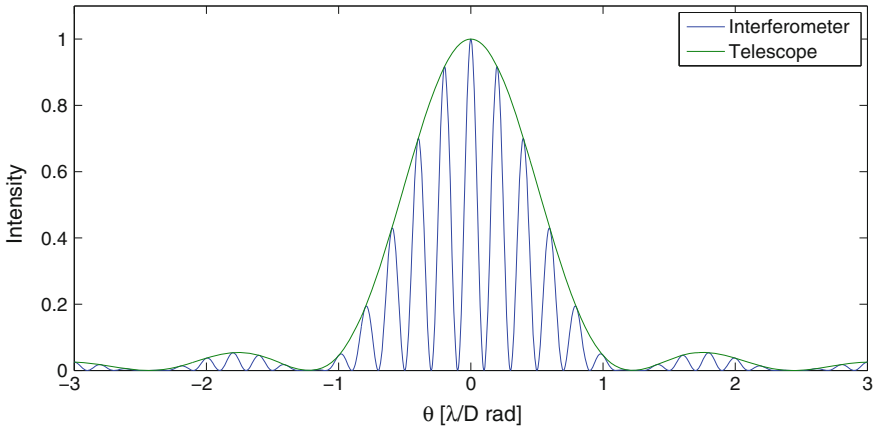

Fig. 2.9 Measured interferogram for a single telescope (*green*) and a two aperture interferometer (*blue*) for a point source. The interferometer fringe pattern is equivalent to the single telescope one multiplied by a cosine given by the baseline separation

Figure 2.9 shows the fringe pattern for a single telescope and an interferometer for a point source, where the baseline separation is $b = 5D$. It can be observed that the resolution of the interferometer is 12 times higher than the resolution of the single aperture if the Rayleigh criterion is used. In interferometry, the resolution of the single aperture is the field of view of the interferometer.

However, if the radiation is not monochromatic one has to consider each frequency separately and add the resulting fringe patterns, which have different separation (λ/b) between maxima. In this situation, the visibility fringes 'wash out', limiting the field of view of the interferometer. If the bandwidth is $\Delta\lambda$, the field of view is given by

$$\Delta\theta = \frac{\lambda}{b}\frac{\lambda}{\Delta\lambda} \tag{2.30}$$

which is the product of the angular (or spatial) resolution and the resolving power $R = \lambda/\Delta\lambda$.

Another quantitative parameter is the fringe contrast, which historically is called *visibility amplitude*. For a 2 telescope interferometer it is calculated as

$$V = \frac{I_{max} - I_{min}}{I_{max} + I_{min}} \tag{2.31}$$

where I_{max} and I_{min} are the maximum and minimum intensity of the fringes, respectively. This value will approach zero if the two beams are incoherent.

2.2.1.3 Complex Visibility

The output of an interferometer are the so-called *complex visibilities*, also called spatial coherence function. When observing an object with an interferometer, the light intensity I is the result of the superposition of electromagnetic waves coming from the apertures. Considering an instrument with two apertures P_1 and P_2, the corresponding electric fields at the apertures are $E_1(t)$ and $E_2(t)$, respectively. At the recombination point Q, the intensity of the recombined signal is

$$I(Q,\tau) = \langle |E_1(t) + E_2(t+\tau)|^2 \rangle_t \tag{2.32}$$

where the time lag τ is caused by the internal light path length difference from each aperture to Q and $\langle\rangle_t$ denotes time average. If one defines the mutual coherence function $\Gamma_{1,2}(\tau)$ as

$$\Gamma_{1,2}(\tau) = \langle E_1(t) E_2^*(t+\tau) \rangle_t \tag{2.33}$$

at recombination point the intensity can be written as

$$\begin{aligned} I(Q,\tau) &= \Gamma_{1,1}(0) + \Gamma_{2,2}(0) + \Gamma_{1,2}(\tau) + \Gamma_{1,2}^*(\tau) \\ &= \Gamma_{1,1}(0) + \Gamma_{2,2}(0) + 2\Gamma_{1,2}^{(r)}(\tau) \end{aligned} \tag{2.34}$$

where $\Gamma_{1,2}^{(r)}(\tau)$ is the real part of $\Gamma_{1,2}(\tau)$, $\Gamma_{1,1}(0) = I_1$ and $\Gamma_{2,2}(0) = I_2$. The interferogram is contained in $\Gamma_{1,2}(\tau)$, and for $\tau = 0$, this is the complex visibility, which is basically the quantity that a Young's double slit experiment measures.

The Van-Cittert-Zernike theorem describes the relation between the complex visibility of an object and its brightness distribution on the plane of the sky. It states that for sources in the far field the normalised value of the spatial coherence function (or complex visibility) is equal to the Fourier transform of the normalised sky brightness distribution. If a source with a brightness distribution $I(\boldsymbol{\theta})$, where $\boldsymbol{\theta} = (\theta_x, \theta_y)$ are the coordinates on the sky plane Ω, illuminates the two apertures connected with the baseline vector $\mathbf{b} = (b_x, b_y)$, the wavenumber dependent spatial coherence function is

$$\frac{V(\mathbf{b})}{V(0)} = \frac{\Gamma_{1,2}(\boldsymbol{b}, \nu)}{\Gamma_{1,2}(0, \nu)} = \frac{\int_\Omega I(\boldsymbol{\theta}, \nu) \exp[-i2\pi\nu\boldsymbol{\theta} \cdot \boldsymbol{b}] d\theta^2}{\int_\Omega I(\boldsymbol{\theta}, \nu) d\theta^2} \tag{2.35}$$

where $\boldsymbol{\theta} \cdot \boldsymbol{b}$ is the projection of the baseline vector on the sky plane. Using spatial frequency notation, this is $u = b_x/\lambda$ and $v = b_y/\lambda$, the normalised complex visibility is

$$V_{norm}(u, v) = \frac{\int_\Omega I(\boldsymbol{\theta}, \nu) \exp[-i2\pi(u\theta_x + v\theta_y)] d\theta^2}{\int_\Omega I(\boldsymbol{\theta}, \nu) d\theta^2} \tag{2.36}$$

The components u and v are the components of the baseline vector between two sampling points projected onto a plane perpendicular to the source direction and measured in wavelengths. It can be observed that by inverse Fourier transforming one can retrieve the source spatial structure if the uv-plane (the Fourier space) has been sampled suitably.

2.2.2 Observability and UV-Coverage

When observing with a stellar interferometer, the efficiency and quality of an observation depends on the sampling of the uv-plane, which is defined by the baseline range and position, the quantity of interest being the projected baseline vector on the sky (Ségransan 2007). For ground based interferometers, two parameters are usually taken into account for the filling of the uv-plane: the Earth rotation and the number of telescopes of the interferometer (Thompson et al. 1986; Millour 2008). By taking advantage of the Earth rotation the uv-tracks become ellipses. The link between the baseline position and its projection on the sky is given by

$$\begin{pmatrix} u \\ v \\ w \end{pmatrix} = \frac{1}{\lambda} \begin{pmatrix} \sin(h) & \cos(h) & 0 \\ -\sin(\delta)\cos(h) & \sin(\delta)\cos(h) & \cos(\delta) \\ \cos(\delta)\cos(h) & -\cos(\delta)\sin(h) & \sin(\delta) \end{pmatrix} \begin{pmatrix} X \\ Y \\ Z \end{pmatrix} \tag{2.37}$$

where (X, Y, Z) represent the terrestrial coordinate system for the antenna position as described in Thompson et al. (1986), and δ and h are the declination and hour angle of the phase reference position. Then the elliptical uv-tracks when observing an object of declination δ are

$$u^2 + \left(\frac{v - (Z/\lambda)^2 \cos(\delta)}{\sin(\delta)} \right)^2 = \frac{1}{\lambda^2}(X^2 + Y^2) \tag{2.38}$$

By increasing the number of telescopes N_t, although this is a more expensive solution, the number of available baselines N_b is increased and is given by

$$N_b = \frac{1}{2} N_t (N_t - 1) \tag{2.39}$$

To further increase the uv-sampling one can use multiple spectral bands. Assuming that an object's shape is achromatic with regards to the wavelength, the uv-coverage is increased simply because different wavelengths represent different spatial frequencies for a given baseline (Millour 2008).

As presented before, the measurement of an interferometer is related to the Fourier transform of the object brightness. In order to maximise the efficiency of

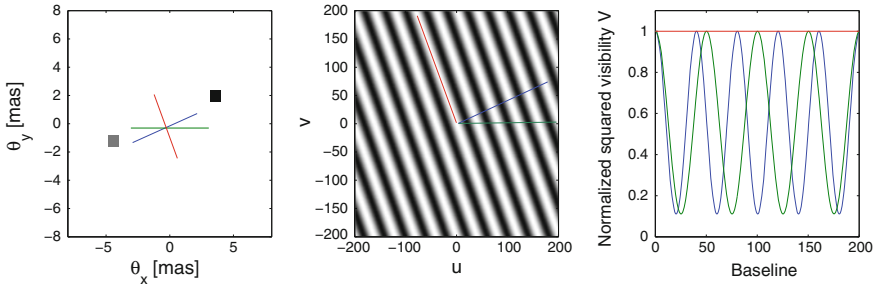

Fig. 2.10 Simulation of an observation of a binary system consisting of 2 unresolved monochromatic point sources separated approximately 9 mas (*left*) and $f = 0.5$. The normalised squared visibility amplitude in units of spatial frequency $1/\lambda$ (*centre*) has a cosine shape given by the source separation. Three baselines have been simulated: aligned with the point sources (*blue*), perpendicular to the line connecting the point sources (*red*), and in an angle between *red* and *blue* (*green*)

an observation, it is important to know the shape and size of the object under study and use it for the selection of the baselines as well as for introducing model fitting to the measured visibilities (Berger and Segransan 2007). For example, if the object is a resolved binary, the brightness can be written as

$$I(\theta_x, \theta_y) = F_1 \delta(\theta_x - \theta_{x,1}, \theta_y - \theta_{y,1}) + F_2 \delta(\theta_x - \theta_{x,2}, \theta_y - \theta_{y,2}) \tag{2.40}$$

where F_1 and F_2 are the fluxes and $(\theta_{x,1}, \theta_{y,1})$ and $(\theta_{x,2}, \theta_{y,2})$ are the angular coordinates of the stars S_1 and S_2. This is sum of two unresolved point sources. In this case, the normalised squared visibility amplitude is

$$|V(u, v)|^2 = \frac{1 + f^2 + 2f \cos[2\pi v(\boldsymbol{\theta} \cdot \boldsymbol{b})]}{(1 + f)^2} \tag{2.41}$$

where $f = F_2/F_1$. Figure 2.10 shows a simulation of an observation of a binary with a separation of approximately 9 mas. Three projected baselines have been considered: blue, aligned with the point sources; red, perpendicular to the line connecting the two point sources; and green, a baseline in between blue and red. It can be observed that the visibility remains constant for the red baseline, because the interferometer 'sees' only one point source. For the blue baseline, the visibility has its maximum frequency. The green baseline presents also a cosine modulation but at a lower frequency. This illustrates the fact than when observing a given object, one has to select the baselines orientation and range accordingly.

2.2.3 Data Synthesis

Once the *uv*-plane has been sampled and so the complex visibilities measured, one could apply the fundamental relationship between the visibility function for a given frequency and the normalised sky brightness distribution, this is

$$I(\theta_x, \theta_y) = \int\int V(u, v) \exp[i2\pi(u\theta_x + v\theta_y)]dudv \tag{2.42}$$

However, in order to extract the source brightness the *uv*-plane should be fully sampled, which is not the case. In practice, one has a sampled version of $V(u, v)$. By performing the inverse Fourier transform of the sampled complex visibility function one obtains the *dirty image* or dirty map

$$I_{dirty}(\theta_x, \theta_y) = \int\int V(u, v)S(u, v) \exp[i2\pi(u\theta_x + v\theta_y)]dudv \tag{2.43}$$

$$= B_{dirty}(\theta_x, \theta_y) * I_{norm}(\theta_x, \theta_y) \tag{2.44}$$

where $S(u, v)$ is the sampling function, which is 1 where the *uv*-plane is sampled and zero otherwise. In this equation, $B_{dirty}(\theta_x, \theta_y)$ is the *dirty beam* and is simply the PSF of the interferometer, which is the Fourier transform of the sampling function

$$B_{dirty}(\theta_x, \theta_y) = \int\int S(u, v) \exp[i2\pi(u\theta_x + v\theta_y)]dudv \tag{2.45}$$

Since the $B_{dirty}(\theta_x, \theta_y)$ is known because it depends on the telescopes positions, recovering the image $I(\theta_x, \theta_y)$ can be accomplished via deconvolution.

Different deconvolution algorithms have been developed for interferometry (Thiébaut 2009). The most popular ones are CLEAN (Högbom 1974) and the Maximum Entropy Method, MEM (Bryan and Skilling 1980; Gull and Skilling 1984), initially developed for radiointerferometric observations but applicable to the optical/IR domain.

In this thesis the CLEAN algorithm is used for the data synthesis of Double Fourier Modulation data and is described in detail in Chap. 5. In general terms, it is basically a numerical deconvolving process applied in the (θ_x, θ_y) domain. It is an iterative process, which consist of breaking down the intensity distribution into point source responses, and then replacing each one with the corresponding response to a 'clean' beam, this is, a beam free of side lobes.

In conclusion, when performing interferometric imaging it is crucial to define the optimal *uv*-sampling for the object to be measured, as the number of baselines is limited. In any case, a more populated *uv*-space will increase the angular resolution of the reconstructed image. As presented before, if the object's shape is achromatic with regards to the wavelength, one way to increase the *uv*-sampling is using multiple spectral bands.

2.3 Multi-Fourier Transform Interferometry

Double Fourier Spatio-Spectral Interferometry is the application of a Fourier-transform spectrometer (FTS) to aperture synthesis interferometry. This technique was proposed for the near IR regime by Itoh and Ohtsuka (1986) with a single-pupil interferometry approach, and by Mariotti and Ridgway (1988) with multi-pupil interferometry for high spatial resolution.

Leisawitz et al. (2003) proposed an extension of the FOV by using a focal plane detector array for optical wavelengths, technique called Wide-Field Imaging Interferometry. However, direct detector arrays in the Far Infrared are still expensive and a similar approach is not straightforward.

Ohta et al. (2006) theoretically proposed to apply a Martin-Puplett-type Fourier-transform spectrometer to the aperture synthesis system in millimeter and submillimeter waves. They succeeded in proving that this system is capable of performing broadband imaging observations (Ohta et al. 2007). Also a laboratory prototype spectral-spatial interferometer (Chap. 3) has been constructed to demonstrate the feasibility of the double-Fourier technique at far infrared (FIR) wavelengths (0.15–1 THz) by Grainger et al. (2012).

2.3.1 Basic Principles

Double Fourier Modulation (DFM) is based on the combination of spatial interferometry and Fourier transform spectroscopy simultaneously. As presented earlier in this chapter, a Fourier transform spectrograph is based on the Michelson interferometer, where the light of a source is divided and recombined while delaying one of the optical paths to generate an interferogram. To combine this technique with spatial interferometry, instead of dividing the light from a single telescope one uses two apertures and recombines the incoming light from these two apertures.

Figure 2.11 shows a classical FTS (left) and a spectro-spatial interferometer (right). In the FTS the incoming light is divided at the beamsplitter (BS) and with the movable mirror an optical path difference is introduced. In the spectro-spatial interferometer, by using two telescopes an extra path difference due to the baseline is introduced when the source is not on the line of sight perpendicular to the baseline. When using the two telescope interferometer, due to the division of the spatial wavefront outside the instrument, one has to take into account all the phase changes of the optical elements (Mariotti and Ridgway 1988). Considering that all mirrors introduce a π phase delay and that the beam splitter is ideal and symmetric, this is the phase delay between the transmitted and reflected beam is $\pi/2$, at the detector one measures sine interferograms due to the extra $\pi/2$ phase shift. Because this is the result of the addition of the beam splitter phase ϕ_{BS}, throughout this thesis this value is left as parameter in order to account for beam splitter non-symmetries.

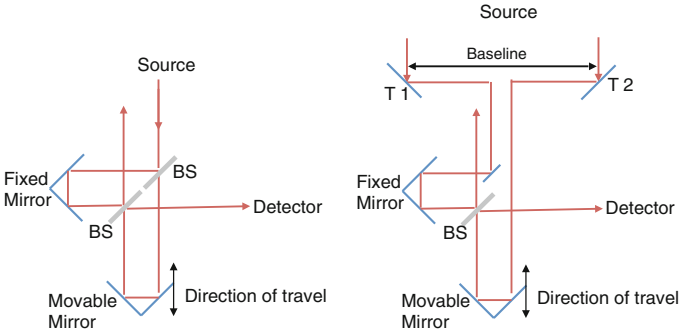

Fig. 2.11 Schematic of a classical FTS (*left*) and a spectro-spatial interferometer (*right*). For the FTS, the incoming light is divided in the first beam splitter and half of it is delayed with the movable mirror before arriving to the second beam splitter where interference occurs. The spectro-spatial interferometer receives light from two telescopes (T1 and T2), and the light travelling from T2 is delayed at the movable mirror before interfering with the light travelling from T1 at the beam splitter, where interference occurs

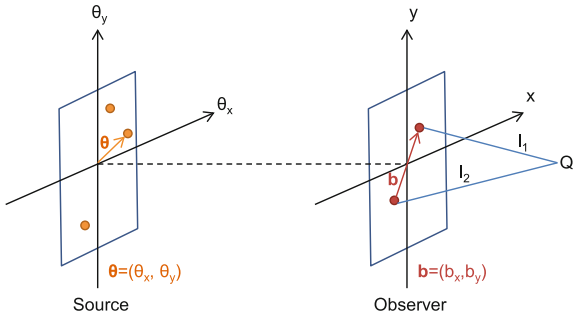

Fig. 2.12 Coordinate system used. The source plane (or sky map in later sections) is assumed to be very far away from the observer plane

Initially one must define the coordinate system, shown in Fig. 2.12 and following the notation of Born and Wolf. The origin of the coordinate system on the source plane is the center of the FOV. The viewer angle of the source from the observer plane is $\boldsymbol{\theta} = (\theta_x, \theta_y)$. The origin of the coordinate system on the observer plane is the center of the baseline ($\boldsymbol{b} = (b_x, b_y)$) that separates the two apertures.

Going back to Eq. 2.34, the complex visibility or spatial coherence function was defined as the mutual coherence function when $\tau = 0$. According to the van-Cittert-Zernike theorem, the normalised spatial coherence function is the Fourier transform of the normalised sky brightness distribution (Eq. 2.35). The temporal coherence function is defined as the mutual coherence function for $b = 0$, and according to the Weiner-Khinchin theorem, the normalised value of the temporal coherence function is equal to the Fourier transform of the normalised spectral energy distribution of the source, this is

$$V(\tau) = \frac{\int B(\omega) \exp(-i\omega\tau) d\omega}{\int B(\omega) d\omega} \tag{2.46}$$

where $\omega = 2\pi f = 2\pi c/\lambda$. With DFM one takes advantage of both aspects of the mutual coherence function.

Considering that $f\tau = \nu\delta$, where δ is the spectroscopical optical path difference due to the movable mirror (as in Eq. 2.9), the measurement of the mutual coherence function by a Multi-Fourier Transform Interferometer of the waves obtained by two apertures for a given baseline and measuring a specific source intensity $I(\boldsymbol{\theta}, \nu)$ is

$$\Gamma(\boldsymbol{b}, \delta) = \int_{\Omega} \left\{ \int I(\boldsymbol{\theta}, \nu) \exp[-i2\pi\nu(\boldsymbol{b} \cdot \boldsymbol{\theta}) + i2\pi\nu\delta + i\phi_{BS}] d\nu \right\} d^2\theta \tag{2.47}$$

and its real part is

$$\Gamma^{(r)}(\boldsymbol{b}, \delta) = \int_{\Omega} \left\{ \int I(\boldsymbol{\theta}, \nu) \cos[-2\pi\nu(\boldsymbol{b} \cdot \boldsymbol{\theta}) + 2\pi\nu\delta + \phi_{BS}] d\nu \right\} d^2\theta \tag{2.48}$$

where Ω is the solid angle subtended by the source, ν is the wavenumber, and δ is the optical path difference between apertures. In this equation the interferometric phase shift $2\pi\nu(\boldsymbol{b} \cdot \boldsymbol{\theta})$ and the spectroscopic modulation $2\pi\nu\delta$ can be easily distinguished.

With Eq. 2.48 one obtains a set of interferograms corresponding to an interferogram per baseline, this is, a spectroscopic measurement for each sampled point in the uv-space. It must be noticed that in this situation, the concept of a spectroscopic zero path difference is not applicable anymore. For example, if the source is a binary consisting of two unresolved point sources, the interferometric phase shift will cause the separation of the two spectroscopic interferograms. This case is similar to the testbed implementation presented in the next chapter.

2.3.2 Data Analysis and Synthesis

To recover the information from the source, a two step process needs to be performed. First, to obtain the spectroscopy-resolved source image one has to perform a Fourier integration of the obtained $\Gamma^{(r)}$ in δ to obtain first the spectrally resolved mutual coherence function, $\hat{\Gamma}(u, v, \nu)$, which in interferometer notation is

$$\hat{\Gamma}(u, v, \nu) = \int_{\Omega} \tilde{I}(\boldsymbol{\theta}, \nu) \exp[-i2\pi(u\theta_x + v\theta_y)] d^2\theta] \tag{2.49}$$

where $u = b_x\nu$, $v = b_y\nu$ and $\tilde{I}$ is a spectrally convolved source intensity distribution, defined as

$$\tilde{I}(\boldsymbol{\theta}, \nu) = \int I(\boldsymbol{\theta}, \nu') 2\delta_0 sinc[2\pi(\nu' - \nu)\delta_0] d\nu' \tag{2.50}$$

The convolution kernel depends on the apodization function, in this case a top-hat function has been used. By Fourier transforming the data in u and v, one obtains source images for various frequencies.

In summary, a DFM system is capable of performing simultaneous measurements of the source brightness distribution and spectrum. In the interferograms, however, the ZPD position is lost, which means that spectroscopy data processing techniques like mathematical apodization and phase correction are not straightforward. Depending on the observation, one can correct the instrumental phase errors by selecting a ZPD for each interferogram separately and computing the slope of the phase from the Fourier transform of a short section around the central fringe area.

2.4 Chapter Summary

In this Chapter the theoretical background that led to the Double Fourier Modulation technique has been presented, this is Fourier Transform Spectroscopy and Stellar Interferometry.

Fourier Transform spectroscopy is based on the Michelson interferometer, with which one can generate and interferogram by dividing the light from a source and recombining it on a beam splitter after delaying one of the optical paths. To obtain the spectra of the source, one has to Fourier transform the interferogram. For a correct detection of the spectral information the sampling of the interferogram is of great importance, because it defines the spectral resolution and the spectral band coverage.

Stellar Interferometry is based on the Young's two slit experiment, where incoming light from a source falls on two apertures (or telescopes) which then are made to interfere onto a screen. The measured quantity is the complex visibility $V(u, v)$. By selecting the position of the telescopes the uv-map is sampled. The brightness distribution on the plane of the source is recovered by Fourier transforming the complex visibility. The aperture separation, or baseline, defines the angular resolution of the interferometer.

The Double Fourier Modulation technique is the combination of Fourier Transform Spectroscopy with Stellar Interferometry: for a given interferometric baseline, one performs an FTS scan. With this technique measurements of the source brightness distribution and spectrum are performed simultaneously.

References

J.P. Berger, D. Segransan, An introduction to visibility modeling. New Astron. Rev. **51**(8), 576–582 (2007)

M. Born, E. Wolf, *Principles of Optics* (1999)

R.K. Bryan, J. Skilling, Deconvolution by maximum entropy, as illustrated by application to the jet of M87. Mon. Not. RAS **191**, 69–79 (1980)

M.L. Forman, W.H. Steel, G.A. Vanasse, Correction of asymmetric interferograms obtained in fourier spectroscopy. J. Opt. Soc. Am. **56**(1), 59–61 (1966). doi:10.1364/JOSA.56.000059. http://www.opticsinfobase.org/abstract.cfm?URI=josa-56-1-59

J.W. Goodman, *Introduction to Fourier optics* (2005)
W.F. Grainger, R. Juanola-Parramon, P.A.R. Ade, M. Griffin, F. Liggins, E. Pascale, G. Savini, B. Swinyard, Demonstration of spectral and spatial interferometry at THz frequencies. Appl. Opt. **51**(12), 2202–2211 (2012). doi:10.1364/AO.51.002202. http://ao.osa.org/abstract.cfm?URI=ao-51-12-2202
P.R. Griffiths, J.A. de Haseth, *Fourier Transform Infrared Spectrometry*, 2nd edn. (Wiley, 2007)
S.F. Gull, J. Skilling, Maximum entropy method in image processing. Commun. Radar Signal Process. IEE Proc. F **131**(6), 646–659 (1984). ISSN 0143-7070. doi:10.1049/ip-f-1:19840099
C. Haniff, An introduction to the theory of interferometry. New Astron. Rev. **51**(8), 565–575 (2007)
E. Hecht, *Optics*, 4th edn. (2001)
J.A. Högbom, Aperture synthesis with a non-regular distribution of interferometer baselines. Astron. Astrophys. Suppl. **15**(1974), 417–426 (1974)
K. Itoh, Y. Ohtsuka, Fourier-transform spectral imaging: retrieval of source information from three-dimensional spatial coherence. J. Opt. Soc. Am. A **3**(1), 94–100 (1986). doi:10.1364/JOSAA.3.000094. http://josaa.osa.org/abstract.cfm?URI=josaa-3-1-94
P.R. Lawson (ed.), *Principles of Long Baseline Stellar Interferometry* (2000)
D.T. Leisawitz, B.J. Frey, D.B. Leviton, A.J. Martino, W.L. Maynard, L.G. Mundy, S.A. Rinehart, S.H. Teng, X. Zhang, in *Wide-field imaging interferometry testbed I: purpose, testbed design, data, and synthesis algorithms*, ed. by M. Shao. Society of Photo-Optical Instrumentation Engineers (SPIE) Conference Series, vol. 4852 of Society of Photo-Optical Instrumentation Engineers (SPIE) Conference Series (2003), pp. 255–267. doi:10.1117/12.460704
J.-M. Mariotti, S.T. Ridgway, Double Fourier spatio-spectral interferometry—combining high spectral and high spatial resolution in the near infrared. Astron. Astrophys. **195**, 350–363 (1988)
A.A. Michelson, *Light Waves and Their Uses*, vol. 3 (The University of Chicago Press, 1903)
A.A. Michelson, XXVIII. Visibility of interference-fringes in the focus of a telescope. Philos. Mag. Ser. 5 **31**(190), 256–259 (1891a). doi:10.1080/14786449108620101. http://www.tandfonline.com/doi/abs/10.1080/14786449108620101
A.A. Michelson, XXXVIII. On the application of interference-methods to spectroscopic measurements. Philos. Mag. Ser. 5 **31**(191), 338–346 (1891b). doi:10.1080/14786449108620117. http://www.tandfonline.com/doi/abs/10.1080/14786449108620117
F. Millour, All you ever wanted to know about optical long baseline stellar interferometry, but were too shy to ask your adviser. New Astron. Rev. **52**(2), 177–185 (2008)
J.D. Monnier, Optical interferometry in astronomy. Rep. Prog. Phys. **66**(5), 789 (2003). http://stacks.iop.org/0034-4885/66/i=5/a=203
R.H. Norton, R. Beer, New apodizing functions for fourier spectrometry. J. Opt. Soc. Am. **66**(3), 259–264 (1976). doi:10.1364/JOSA.66.000259. http://www.opticsinfobase.org/abstract.cfm?URI=josa-66-3-259
I.S. Ohta, M. Hattori, H. Matsuo, Development of a multi-Fourier-transform interferometer: fundamentals. Appl. Opt. **45**, 2576–2585 (2006). doi:10.1364/AO.45.002576
I.S. Ohta, M. Hattori, H. Matsuo, Development of a multi-Fourier-transform interferometer: imaging experiments in millimeter and submillimeter wave bands. Appl. Opt. **46**, 2881–2892 (2007). doi:10.1364/AO.46.002881
A. Quirrenbach, Optical interferometry. Ann. Rev. Astron. Astrophys. **39**, 353–401 (2001). doi:10.1146/annurev.astro.39.1.353
D. Ségransan, Observability and UV coverage. New Astron. Rev. **51**(8), 597–603 (2007)
É. Thiébaut, Image reconstruction with optical interferometers. New Astron. Rev. **53**(11), 312–328 (2009)
A.R. Thompson, J.M. Moran, G.W. Swenson, *Interferometry and Synthesis in Radio Astronomy* (1986)
T. Young, The bakerian lecture: experiments and calculations relative to physical optics. Philos. Trans. R. Soc. Lond. **94**, 1–16 (1804). ISSN 02610523. http://www.jstor.org/stable/107135

http://www.springer.com/978-3-319-29399-8

A Far-Infrared Spectro-Spatial Space Interferometer Instrument Simulator and Testbed Implementation

Juanola-Parramon, R.

2016, XV, 156 p. 100 illus., 72 illus. in color., Hardcover
ISBN: 978-3-319-29399-8